

Poleward Heat Transport in a Barotropic Ocean Model

XIAOLI WANG, PETER H. STONE, AND JOCHEM MAROTZKE

Center for Global Change Science, Massachusetts Institute of Technology, Cambridge, Massachusetts

(Manuscript received 22 November 1993, in final form 20 June 1994)

ABSTRACT

A barotropic ocean circulation model coupled to a mixed-layer temperature equation is used to study the poleward heat transport by the horizontal wind-driven ocean currents. Through scaling analyses, two different regimes of the heat transport are found, characterized by $\lambda \rightarrow \infty$ and $\lambda \rightarrow 0$, respectively, where λ is the ratio between the ocean advection timescale and the restoring timescale of Newtonian cooling at the air-sea interface. In the regime $\lambda \rightarrow \infty$, the heat transport is proportional to λ^{-1} and to the second power both of the basin east-west width and of the magnitude of wind stress curl. In the regime $\lambda \rightarrow 0$, the heat transport is proportional to λ and to the basin width, and insensitive to the magnitude of wind stress curl. The heat transport is a maximum for intermediate values of λ , and the numerical experiments show that a restoring timescale of 5 months maximizes the heat transport for a barotropic square basin 500 m deep and 4000 km wide (North Atlantic size). The corresponding maximum heat transport is about 0.32 PW. If the basin width is doubled (North Pacific size), the maximum poleward heat transport by the modeled ocean currents is estimated to be 0.73 PW. The numerical experiments also show that the heat transport can be underestimated if the model resolution is too coarse—for example, for a horizontal resolution of $4^\circ \times 4^\circ$, the heat transport is underestimated by about 50%.

1. Introduction

It is widely accepted that the ocean plays an important role in moderating the climate system. In addition to the heat buffer effect on the climate, the ocean circulation transports substantial heat poleward. This poleward heat transport influences the latitudinal climate variations and climate sensitivity, and thus has long been recognized as a key part of the global climate system. Since the measurements of oceanic currents remain difficult, few heat transport estimates based on the hydrographic data are reliable, or even available so far. Probably the most accurate in situ measurements of heat transport are those at 24°N , which are 1.2 ± 0.3 PW for the Atlantic (Hall and Bryden 1982; hereafter HB) and 0.76 ± 0.3 PW for the Pacific (Bryden et al. 1991). Inverse model estimates give a similar heat transport across 24°N in the Atlantic (Rintoul and Wunsch 1991; Roemmich and Wunsch 1985).

In numerical oceanic models, however, the heat transport is generally much smaller than observed. In particular, the Geophysical Fluid Dynamics Laboratory oceanic general circulation model (GCM) with resolution of 3.75° longitude by 4.0° latitude shows maximum North Atlantic heat transport of typically one-half of HB's result (England 1993; Manabe and Stouffer

1988; Bryan and Lewis 1979). A higher resolution of $2/5^\circ$ by $1/3^\circ$ improves the maximum heat transport to 0.6 PW for the North Atlantic, but this is still too weak (Bryan and Holland 1989). In ocean-atmosphere coupled GCM experiments (Manabe and Stouffer 1988), the surface fluxes have been artificially adjusted in order to simulate the present climate. The weakness of oceanic heat transports in GCMs may be one of the major reasons for the "climate drift" occurring in climate models without flux adjustments.

An important implication from the in situ measurements is that the mechanism of heat transport in the North Atlantic is quite different from that in the North Pacific. For the Atlantic, because of the North Atlantic Deep Water formation, the heat is transported poleward by the combination of the wind-driven circulation and the meridional overturning circulation. The whole picture is a three-dimensional diagonal cell that has both horizontal and vertical components (HB). By contrast, in the North Pacific, which lacks deep water formation, the poleward heat transport appears to be primarily by the wind-driven circulation in the upper 700 m of the ocean (Bryden et al. 1991). Since the relative importance of the wind-driven circulation is so different in these two oceanic basins, it is worthwhile to study the sensitivity of the heat transport in the framework of a simple process model, which retains the essential features of the wind-driven circulation while excluding the meridional overturning circulation.

Corresponding author address: Dr. Peter Stone, Department of Earth, Atmospheric, and Planetary Sciences, Room 54-1718, Massachusetts Institute of Technology, Cambridge, MA 02139.

In this study, we assess the potential contribution of the wind-driven circulation to the poleward heat transport by using a barotropic model. The dynamical model is numerically solved as an initial value problem. Then the equilibrium velocity field is used to advect the temperature field in a thermodynamical equation. Meanwhile, the air-sea interfacial heat flux is parameterized by a Newtonian law (Haney 1971). The heat transport is determined when the temperature equation reaches equilibrium. Essentially the same model has been used by Bye and Veronis (1980) and Huynh and Veronis (1981) to study heat transport. However, they did not investigate how the transport depends on model resolution or the full dependence of the heat transport on the air-sea heat exchange timescale. We are particularly interested in these dependences since climate GCMs do not yet resolve the western boundary currents and the heat exchange timescale is uncertain (Marotzke 1994).

The model used in this study is described in section 2. The barotropic dynamic model is an extension of the wind-driven gyre-scale model initiated by Bryan (1963) and continued by Veronis (1966), Blandford (1971), Marshall (1984), and Moro (1988). Although the model is crude with no attempt to resolve the vertical structure of the circulation, it includes the basic ingredients of all the wind-driven circulation models: a vorticity source provided by the wind stress curl, a representation of the redistribution of vorticity by ocean currents, and a vorticity sink by friction. The result is a model that is economical to run, so that a large number of experiments can be performed, with a sensitivity which reflects in part that of more complex wind-driven dynamic models.

In section 3, preliminary estimates of the model sensitivity based on scaling arguments are presented. Two different regimes, characterized by $\lambda \rightarrow 0$ and $\lambda \rightarrow \infty$, respectively, are also discussed in that section. Here λ is a nondimensional parameter representing the ratio between the ocean advection timescale and the local air-sea interaction timescale. The sensitivity of the heat transport to changes in various parameters are determined by examining the scaling law and a series of numerical experiments in section 4. The numerical results agree qualitatively with the scaling estimates. A summary and conclusion follow in section 5.

2. Model description

a. Dynamical equation

We consider a barotropic vorticity equation in a 4000 km \times 4000 km square basin on the midlatitude β plane. The model basin corresponds roughly to the North Atlantic between 17° and 55°N; for comparison, the North Atlantic is 5850 km wide at 35°N and 3000 km at 55°N. The model ocean is driven by a surface wind stress curl and retarded by bottom friction and lateral friction (Blandford 1971). For the large-scale flow, the

mass transport tends to be concentrated above the main thermocline (Anderson et al. 1979). To take this into account, the model ocean depth is defined as the depth of the main thermocline rather than that of the ocean. The nondimensional form of the barotropic vorticity equation is given by

$$\frac{\partial \zeta}{\partial t} + \text{Ro} \left(\frac{\partial \psi}{\partial x} \frac{\partial \zeta}{\partial y} - \frac{\partial \psi}{\partial y} \frac{\partial \zeta}{\partial x} \right) + \frac{\partial \psi}{\partial x} = (\nabla \times \tau)_z + \frac{\text{Ro}}{\text{Re}} \nabla^2 \zeta - \epsilon \zeta, \quad (1)$$

where (dimensional values are denoted by asterisks)

$$\psi_x = \frac{1}{HV_s^*} \int_{-H}^0 v^* dz^* \quad (2)$$

$$\psi_y = \frac{1}{HV_s^*} \int_{-H}^0 u^* dz^*,$$

$$\psi \text{ is the transport streamfunction} \quad (3)$$

$$(x^*, y^*) = L(x, y) \quad (4)$$

$$t^* = (\beta L)^{-1} t \quad (5)$$

$$(u^*, v^*) = V_s^*(u, v), \text{ horizontal velocities} \quad (6)$$

$$V_s^* = \frac{|(\nabla \times \tau)_z^*|}{\rho_0 \beta H}, \quad (7)$$

$$\text{Ro} = \frac{V_s^*}{\beta L^2}, \text{ Rossby number} \quad (8)$$

$$\text{Re} = \frac{V_s^* L}{A_H}, \text{ Reynolds number} \quad (9)$$

$$\epsilon = \frac{K}{\beta L}, \text{ bottom friction coefficient} \quad (10)$$

$$\zeta = \nabla^2 \psi, \text{ (relative vorticity);} \quad (11)$$

L is the basin's east-west extent, ρ_0 is an oceanic reference density, H is the barotropic ocean depth, and V_s^* is the magnitude of the interior velocity, given by the Sverdrup relation.

The standard values of model constants are as follows: the barotropic ocean depth $H = 500$ m and the horizontal basin scale $L = 4000$ km; the magnitude of the wind stress curl $|(\nabla \times \tau)_z^*| = 2.0 \times 10^{-7} \text{ N m}^{-3}$ (Trenberth 1989); and $\beta = 2 \times 10^{-11} \text{ m}^{-1} \text{ s}^{-1}$; thus, $V_s^* = 0.02 \text{ m s}^{-1}$.

The zonal wind stress curl has a pattern that corresponds to an asymmetric subtropical gyre and subpolar gyre similar to that used by Moro (1988). Its profile (Fig. 1) is given by an analytic expression that captures the major features of the observed zonally averaged wind stress:

$$(\nabla \times \tau)_z = -\{1 + \exp[-50(y - 0.72)^2]\} \times [\sin(2\pi y) + 0.25 \sin(\pi y)]/1.65. \quad (12)$$

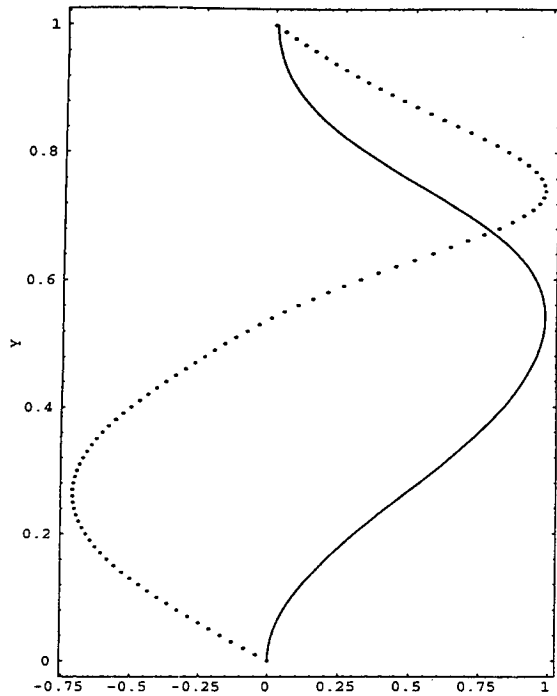


FIG. 1. The profile of wind stress (shown by the solid line) and its curl (by the dashed line) used in this study. All variables are in non-dimensional units.

The scales of the western boundary layer can be deduced by matching the beta term with either the non-linear term or the frictional terms:

- 1) $\delta_I = \text{Ro}^{1/2}$, inertial boundary layer width
- 2) $\delta_M = (\text{Ro}/\text{Re})^{1/3}$, lateral frictional boundary layer width
- 3) $\delta_F = \epsilon$, bottom frictional boundary layer width.

In our numerical calculations,

$$\delta_F \leq \delta_I \leq \delta_M. \quad (13)$$

A no-slip boundary condition is applied in the model. The model is spun up from a state at rest and integrated for 10 months, which is sufficient to reach equilibrium.

b. Coupling with the thermodynamic equation

The model ocean is allowed to transport heat by the simulated barotropic wind-driven currents. We make the simplifying assumption that the temperature is well mixed throughout the barotropic layer of depth H . The heat fluxes across the air-sea interface are parameterized following Haney (1971). Changes in the oceanic state are not allowed to feed back on the atmosphere. The surface heat flux into the ocean is approximated by a linear Newtonian law,

$$F = \rho_0 C \frac{(T_A - T_0)}{\tau_d} H, \quad (14)$$

where T_0 is the ocean temperature and T_A is an apparent atmospheric temperature, which includes the effects of evaporation, sensible heat flux, and solar and terrestrial radiation. We prescribe the distribution of T_A to be a linear function of latitude varying from 28°C at the southern boundary to 8°C at the northern boundary. The restoring timescale τ_d is the timescale of the air-sea interface heat exchange, and C the specific heat of water.

The nondimensional temperature equation for a barotropic flow in a well-mixed layer is

$$\frac{1}{\text{Ro}} \frac{\partial T_0}{\partial t} + u \frac{\partial T_0}{\partial x} + v \frac{\partial T_0}{\partial y} = \lambda (T_A - T_0) + K_H \nabla^2 T_0, \quad (15)$$

where

$$\lambda = \frac{L/V_s^*}{\tau_d} \quad (16)$$

represents the ratio between the oceanic advection timescale in the basin interior and the air-sea heat exchange timescale. For our standard parameter choices, the advection timescale is

$$t = \frac{L}{V_s^*} = \frac{4000 \text{ km}}{0.02 \text{ m s}^{-1}} = 6.3 \text{ yr}. \quad (17)$$

In (15) K_H is an inverse Peclet number,

$$K_H = \frac{K_H^*}{V_s^* L}, \quad (18)$$

where K_H^* is the diffusion coefficient. The dependence of the heat transport on K_H has been studied by Bye and Veronis (1980). Here we chose $K_H^* = 8 \times 10^2 \text{ m}^2 \text{ s}^{-1}$, so that the magnitude of the diffusive heat transport is typically much smaller than the dynamical heat transport. Therefore, in most cases, the diffusion term is maintained only for its effect on numerical stability, not for physical considerations.

An insulated wall is assumed as the lateral boundary condition. The initial condition of sea surface temperature is $T_0 = T_A$. The integration time is about 6 years, sufficient for the temperature field to reach equilibrium.

3. Scaling laws for the heat transport

Before presenting the numerical solutions for the heat transport, we derive scaling laws for the heat transport in equilibrium. Various characteristic scales are defined as follows:

- L : the basin size in east-west direction
- L_y : the basin size in south-north direction
- L_b : the western boundary layer width
- V_b : the western boundary layer current speed
- V_s : the interior flow speed
- T_b : SST in the western boundary layer

T_s : SST in the interior region.

The mass conservation equation gives

$$V_s(L - L_b) = V_b L_b. \quad (19)$$

Since $L \gg L_b$, it follows that $V_b \gg V_s$ and $V_s L \approx V_b L_b$.

From Eq. (19) it follows that the heat transported by the currents across a latitude in the basin, Q , can be approximated by

$$Q = \rho_0 C H \int_0^L v^* T dx^* \sim [V_b L_b (T_b - T_s)] \rho_0 C H. \quad (20)$$

Thus, the heat transport is proportional to the mass transport in the boundary layer and the zonal sea surface temperature difference between the boundary layer and the interior. If the poleward boundary current is warmer than the return southward interior flow, heat will be transported poleward.

We now apply perturbation methods to discuss the two regimes characterized by $\lambda \rightarrow \infty$ and $\lambda \rightarrow 0$, respectively. Similar perturbation analyses were carried out by Bye and Veronis (1980). However, they generally assumed $K_H \gg 1$, whereas we will assume $K_H \ll 1$, and they did not use their analyses to investigate how the heat transport depends on λ .

a. Regime I: $\lambda \rightarrow \infty$

Since λ is the ratio between the ocean advection timescale and the restoring timescale, as $\lambda \rightarrow \infty$, the local air-sea heat exchange takes place in a much shorter time than that of the ocean advection process, and the SST distributions are strongly restored to the zonally uniform pattern of T_A except in the western boundary layer.

The magnitude of the heat transport in the neighborhood of this limit can be derived by using a perturbation method. For $\lambda \rightarrow \infty$, the sea surface temperature T_0 can be expanded around T_A ,

$$T_0 = T_A + T', \quad (21)$$

where T' is a small perturbation term. Substituting into Eq. (15), assuming equilibrium, neglecting small terms of $O(T')$, assuming that $K_H \ll 1$ and that $\lambda T'$ is $O(1)$ as $\lambda \rightarrow \infty$, we obtain

$$v \frac{\partial T_A}{\partial y} = -\lambda T'. \quad (22)$$

The dimensional form of Eq. (22) is

$$v^* \frac{\partial T_A}{\partial y^*} = -\frac{1}{\tau_d} T'. \quad (23)$$

Multiplying Eq. (23) by v^* and integrating in x^* from 0 to L gives

$$-\tau_d \frac{\partial T_A}{\partial y^*} \int_0^L v^{*2} dx^* = \int_0^L v^* T' dx^*. \quad (24)$$

The right side of Eq. (24) is proportional to the heat transport in the limit $\lambda \rightarrow \infty$. Using Eq. (19), we estimate

$$\int_0^L v^{*2} dx^* \sim V_b L_b (V_b + V_s) \approx V_b^2 L_b \approx \frac{(V_s L)^2}{L_b}. \quad (25)$$

The nondimensional scale of the western boundary layer is the maximum of δ_I , δ_M , and δ_F . Thus, the western boundary layer width can be written in one of the following three forms, depending on the relative magnitude of δ_I , δ_M , and δ_F ,

$$L_b = \begin{cases} \delta_I L = \text{Ro}^{1/2} L = \left(\frac{V_s^*}{\beta} \right)^{1/2} \\ \delta_M L = \left(\frac{\text{Ro}}{\text{Re}} \right)^{1/3} L = \left(\frac{A_H}{\beta} \right)^{1/3} \\ \delta_F L = \epsilon L = \frac{K}{\beta}. \end{cases} \quad (26)$$

Note that in all the three cases, the western boundary layer width L_b is independent of the basin width L . We substitute Eqs. (7), (24), (25), and (26) back into Eq. (20) to obtain the scale of the heat transport Q in terms of external parameters:

$$Q = -\frac{C \tau_d}{\rho_0 \beta^2 H} \frac{\partial T_A}{\partial y^*} |(\nabla \times \tau)_z^*|^2 L^2 \times \begin{cases} \left(\frac{\beta^2 \rho_0 H}{|(\nabla \times \tau)_z^*|} \right)^{1/2}, & \delta_I \geq (\delta_M, \delta_F) \\ \left(\frac{\beta}{A_H} \right)^{1/3}, & \delta_M \geq (\delta_I, \delta_F) \\ \left(\frac{\beta}{K} \right), & \delta_F \geq (\delta_M, \delta_I). \end{cases} \quad (27)$$

The first notable result of Eq. (27) is that the heat transport is proportional to the second power of the basin width. The physical basis for this sensitivity can be explained in terms of scaling variables. Imagine that the model basin width is doubled, while all other parameters (e.g., wind stress curl, β parameter, diffusion parameter, etc.) remain the same. The Sverdrup mass transport will also be doubled in response to the increased basin width. But the boundary layer width is unchanged because it is independent of the basin size. Therefore, the velocity in the western boundary layer is expected to be twice as large as before. The deviation of the surface temperature from the prescribed T_A value in the western boundary layer increases with the strengthening of the boundary current [see Eq. (23)]. Thus, the heat transport is four times as large when the basin width is doubled.

Another result from Eq. (27) is that the heat transport is essentially proportional to the second power of the magnitude of wind stress curl. A similar explanation

can be given as above. In fact, Bryan and Cox (1968) have observed sensitivity to the magnitude of the wind stress curl in their fully three-dimensional primitive equation model. Equation (27) also indicates that the heat transport is proportional to the restoring timescale and to the meridional gradient of the apparent atmospheric temperature T_A , which will be discussed further in section 4.

b. Regime II: $\lambda \rightarrow 0$

In this regime, the timescale of the advection process is much smaller than the local air-sea heat exchange timescale. In the limit $\lambda \rightarrow 0$, Eq. (15) reduces to

$$\frac{1}{\text{Ro}} \frac{\partial T_0}{\partial t} + u \frac{\partial T_0}{\partial x} + v \frac{\partial T_0}{\partial y} = K_H \nabla^2 T_0. \quad (28)$$

Since Ro , u , v , and K_H are specified quantities and the boundaries are insulating walls, diffusion must cause the solution to Eq. (28) to become homogeneous as $t \rightarrow \infty$; that is, $T_0 \rightarrow \text{const}$. The value of this constant is determined by an integral constraint on the total solution for T_0 . In equilibrium, because there is no transport or diffusion of heat through the basin's walls, the solution of the full Eq. (15), for any nonzero λ , must satisfy

$$\frac{1}{A} \iint T_0 dx^* dy^* = \frac{1}{A} \iint T_A dx^* dy^* \equiv \bar{T}_A, \quad (29)$$

where A is the area of the basin and \bar{T}_A is the basin-averaged apparent atmospheric temperature. Since this result is independent of λ , we identify \bar{T}_A as the constant temperature that T_0 must approach as $t \rightarrow \infty$ in the limit $\lambda \rightarrow 0$. Thus, for small λ we expand T_0 as

$$T_0 = \bar{T}_A + T', \quad (30)$$

where T' is a small temperature perturbation of order λ . We note that there is no heat transport if $T' = 0$, because of mass conservation.

Now substituting Eq. (30) into Eq. (15), assuming equilibrium and that $K_H \ll 1$, and neglecting the small terms, $\lambda T'$ and $K_H \nabla^2 T'$, we have, to first order in λ ,

$$\frac{\partial(uT')}{\partial x} + \frac{\partial(vT')}{\partial y} = \lambda(T_A - \bar{T}_A). \quad (31)$$

Now we integrate Eq. (31) in x , with the boundary conditions $u = 0$ at $x = 0, 1$ to obtain

$$\frac{\partial}{\partial y} \int_0^1 v T' dx = \lambda(T_A - \bar{T}_A). \quad (32)$$

The dimensional form of Eq. (32) is

$$\frac{\partial}{\partial y^*} \int_0^L v^* T' dx^* = \frac{L}{\tau_d} (T_A - \bar{T}_A). \quad (33)$$

Integrating Eq. (33) in y^* , we obtain the poleward heat transport Q at latitude y_m ,

$$Q(y_m) = \rho_0 CH \frac{L}{\tau_d} \int_0^{y_m} (T_A - \bar{T}_A) dy^*. \quad (34)$$

Since T_A is a linear function of y^* , we have

$$T_A = \bar{T}_A - \frac{\partial T_A}{\partial y^*} \left(y^* - \frac{1}{2} L_y \right). \quad (35)$$

We substitute Eq. (35) into Eq. (34) to obtain

$$Q(y_m) = \rho_0 CH \frac{L}{2\tau_d} \frac{\partial T_A}{\partial y^*} y_m (L_y - y_m). \quad (36)$$

The above result indicates that regime II is quite different from regime I. Now, the dependence on the wind stress curl vanishes. The heat transport depends on τ_d , the basin width and the distribution of T_A . As $\tau_d \rightarrow \infty$, when diffusion is weak, the isotherms of sea surface temperature T_0 tend to follow the closed streamlines. The insensitivity of the heat transport to the change of wind stress curl can be explained in a Lagrangian view. Consider a parcel on a certain streamline; the larger its velocity, the longer distance it can travel before its temperature is modified by the local air-sea heat flux, and therefore the smaller the temperature difference between the west and the east of the basin. An increase (or decrease) of the current velocity is always compensated by a decrease (or increase) in the zonal temperature differential, and the heat transport remains constant. Similarly, the heat transport is reduced to a first power dependence on the basin width, rather than the second power of regime I. In both regimes, the heat transport is proportional to the meridional gradient of the apparent atmospheric temperature T_A . Since in both limits of λ the heat transport approaches zero, the heat transport must be maximized by an intermediate value of λ .

In the next section, we present numerical solutions and compare the numerical results with the scaling laws discussed here. We will see that the agreement is favorable.

4. Numerical solution and sensitivity study

a. The reference solution

The reference case has a resolution of 60 km in both latitudinal and longitudinal directions. There are four nondimensional parameters in the model that need to be specified: Ro , Re , ϵ , and λ . For $L = 4000$ km and $|(\nabla \times \tau)_z^*| = 2.0 \times 10^{-7} \text{ N m}^{-3}$, the Rossby number is calculated to be 6.25×10^{-5} , and the inertial boundary layer scale is $\delta_I = 7.9 \times 10^{-3}$. Blandford (1971) reported that retaining a small bottom friction rapidly damps numerical oscillations. Thus, we use a small ϵ , 10^{-3} , and the frictional boundary layer scale is $\delta_F = 10^{-3}$. The Reynolds number is less easily specified, but, as we will show later, the maximum heat transport is not sensitive to the Reynolds number. In the reference solution, we let $\text{Re} = 90$, and the corresponding

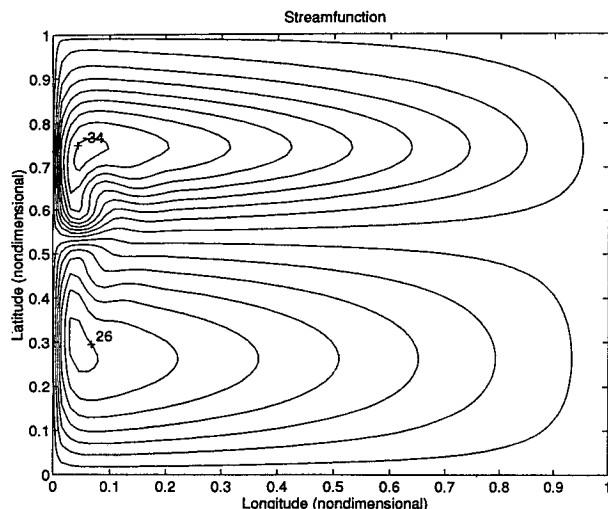


FIG. 2. The asymptotic steady streamfunction of the reference solution with $Ro = 6.25 \times 10^{-5}$, $Re = 90$, $\epsilon = 10^{-3}$; CI (contour interval): 4 Sv ($Sv \equiv 10^6 \text{ m}^3 \text{ s}^{-1}$).

lateral frictional boundary layer scale is $\delta_M = 8.8 \times 10^{-3}$.

The equilibrium streamfunction for the reference solution is displayed in Fig. 2. The modeled mass transport of the subtropical gyre is about 26 Sv ($Sv \equiv 10^6 \text{ m}^3 \text{ s}^{-1}$), which is close to Gulf Stream mass transport at the Florida Strait (HB). An air-sea heat exchange timescale of 5 months ($\lambda = 20$) is used in the reference solution, and as will be discussed later, the heat transport is maximized by this value of λ . Figure 3 shows the sea surface temperature field at equilibrium, which exhibits strong thermal fronts along the western boundary and in the recirculation region.

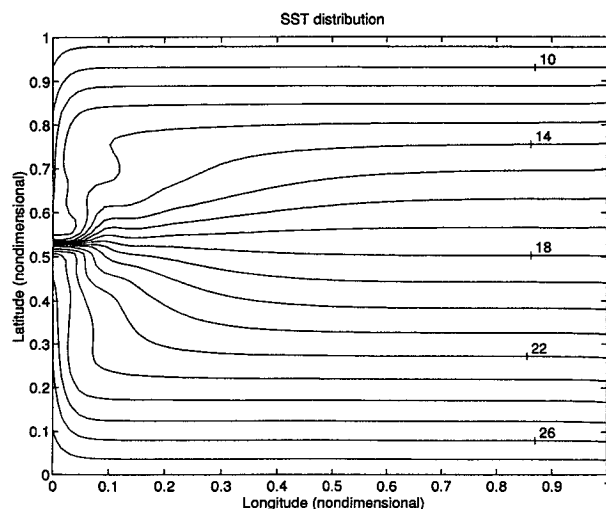


FIG. 3. The equilibrium sea surface temperature simulated in the reference run; CI: 1°C .

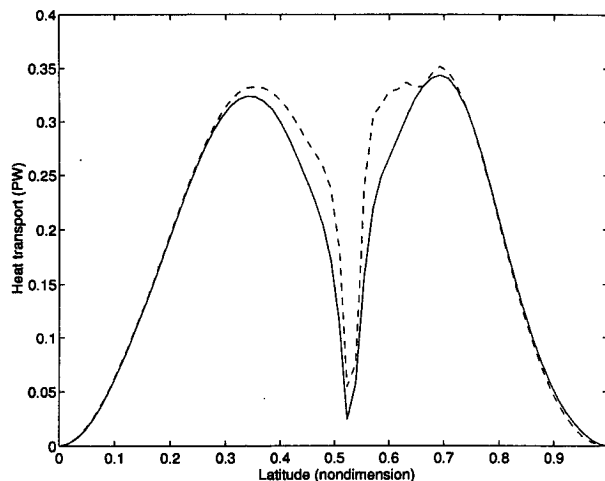


FIG. 4. The simulated poleward heat transport as a function of latitude in the reference solution (solid line) and the high Reynolds number solution (dashed line).

The heat transport across latitude belts is displayed in Fig. 4 (solid line). The extremely small heat transport in the recirculation region is associated with the small meridional flow across the two gyres' interface. We speculate that in a baroclinic model, mesoscale eddies would play an important role in transferring heat across this jet. Figure 4 also shows that the maximum heat transport by the modeled subtropical gyre is about 0.32 PW in the reference solution.

The experiments performed in this study are listed in Table 1, which includes variations of Reynolds number, λ , model resolution, wind stress curl, T_A pattern, and the basin width. Except where indicated, the parameters are the same as in the reference solution.

b. Sensitivity to Reynolds number and λ

The dynamics of the model is sensitive to the Reynolds number. For large Re , the inertial boundary layer

TABLE 1. Sensitivity experiments for various parameters: Reynolds number, model resolution, wind stress curl, T_A , and basin width. The maximum heat transport by the subtropical gyre has unit of PW ($= 10^{15} \text{ W}$).

Experiment number	Description	Maximum heat transport
1	Reference solution ($Re = 90$)	0.32
2	High Reynolds number ($Re = 720$)	0.33
3	Resolution of $400 \text{ km} \times 400 \text{ km}$	0.18
4	Resolution of $30 \text{ km} \times 30 \text{ km}$	0.34
5	Halving the wind stress curl	0.16
6	Doubling the wind stress curl	0.77
7	Reducing $\partial T_A / \partial y$ by 20%	0.26
8	Increasing $\partial T_A / \partial y$ by 20%	0.40
9	Set $\partial T_A / \partial x^* = +5 \times 10^{-7} \text{ }^\circ\text{C m}^{-1}$	0.28
10	Set $\partial T_A / \partial x^* = -5 \times 10^{-7} \text{ }^\circ\text{C m}^{-1}$	0.38
11	Doubling the basin width ($2 \times L$)	0.73

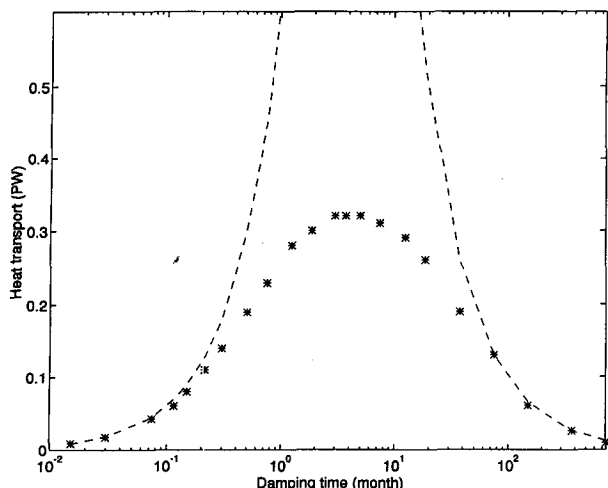


FIG. 5. Variation of the maximum heat transport Q_m with the Newtonian restoring time (in log coordinate). The dashed lines are the scaling results, and asterisks are the numerical results.

scale (δ_I) may exceed the lateral frictional boundary layer scale (δ_M), and the dynamical model becomes highly nonlinear. The threshold value for Re is

$$\delta_M = \delta_I \rightarrow (Re)_0 = Ro^{-1/2} = 126. \quad (37)$$

As the Reynolds number is increased above some value [usually when $Re \gg (Re)_0$], barotropic instability starts to occur and eddies begin to form. Moro (1988) reported that the mass transport of the recirculation is sensitive to changes in Re . However, in this study, emphasis is not on the recirculation region, but near the center of the subtropical gyre where the first maximum in the heat transport is expected. Experiment 2 is designed to determine the sensitivity of the heat transport in this region to high Reynolds number. The model results indicate that the mass transport of the subtropical gyre in experiment 2 ($Re = 720$) and the reference solution ($Re = 90$) are almost identical (not shown here). The difference in the heat transport distributions between these two cases is not significant (as displayed in Fig. 4). Since the dynamical model reaches steady state in a much shorter integration time for low Reynolds number than for high Reynolds number, the low Reynolds number is used for the reference solution.

The scaling laws have indicated that the heat transports decrease to zero in both limits: $\lambda \rightarrow \infty$ and $\lambda \rightarrow 0$. Thus we expect that an intermediate value of λ will maximize the heat transport. Figure 5 displays how the maximum heat transport by the modeled subtropical gyre, Q_m , varies with λ . The two asymptotic limits from the scaling analyses are also plotted in Fig. 5, and are consistent with the numerical results. We see that an air-sea heat exchange timescale of about 4–5 months ($\lambda \approx 20$) maximizes the heat transport in the model. From atmospheric data, Haney (1971) calculated a restoring timescale corresponding to 20 months for an

upper-layer ocean 500-m deep. A discussion of which, if any, restoring timescale is appropriate goes beyond the scope of this paper. We use a Newtonian restoring timescale of 5 months in most experiments because our interest is in assessing the maximum role of the wind-driven circulation in the oceanic heat transport process. However, we note that the heat transport for a 20-month restoring timescale is about 20% less than the maximum value.

c. Sensitivity to model resolution

Oceanic GCMs used in climate modeling usually have coarse resolutions (order of 4° – 5° , e.g., Manabe and Stouffer 1988), which do not resolve the very narrow boundary currents, which are typically 60–100 km wide. It is important to know whether low resolution degrades model heat transport. The coarsest resolution used in our experiments is $400 \text{ km} \times 400 \text{ km}$, which is close to the resolution of many ocean climate models. The model resolution was varied over a broad range, the highest resolution being $30 \text{ km} \times 30 \text{ km}$. The results of Q_m for different model resolutions are displayed in Fig. 6. The maximum heat transport in the coarsest resolution model is only about half of that in the high-resolution model (0.18 PW vs 0.34 PW).

To understand why the coarse resolution model underestimates the heat transport, we plot cross sections along latitude of Q_m for three different resolutions. Figures 7a–c show, in turn, the meridional velocity v^* , the surface temperature T_0 , and the product of v^* and T_0 for experiments 1, 3, and 4. The weak heat transport is associated with the underestimate of the temperature of the western boundary currents in the coarse-resolution model, while the mass transports are almost the same for different resolutions. Figure 6 also indicates

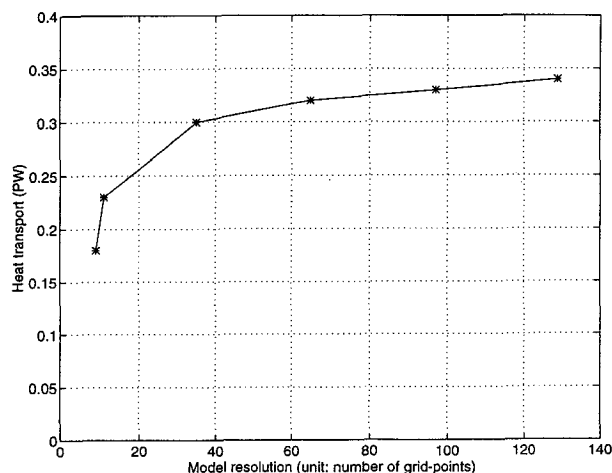


FIG. 6. The maximum heat transport Q_m simulated in the different resolutions of the model. The reference case has 66 grid points. The basin size is $4000 \text{ km} \times 4000 \text{ km}$.

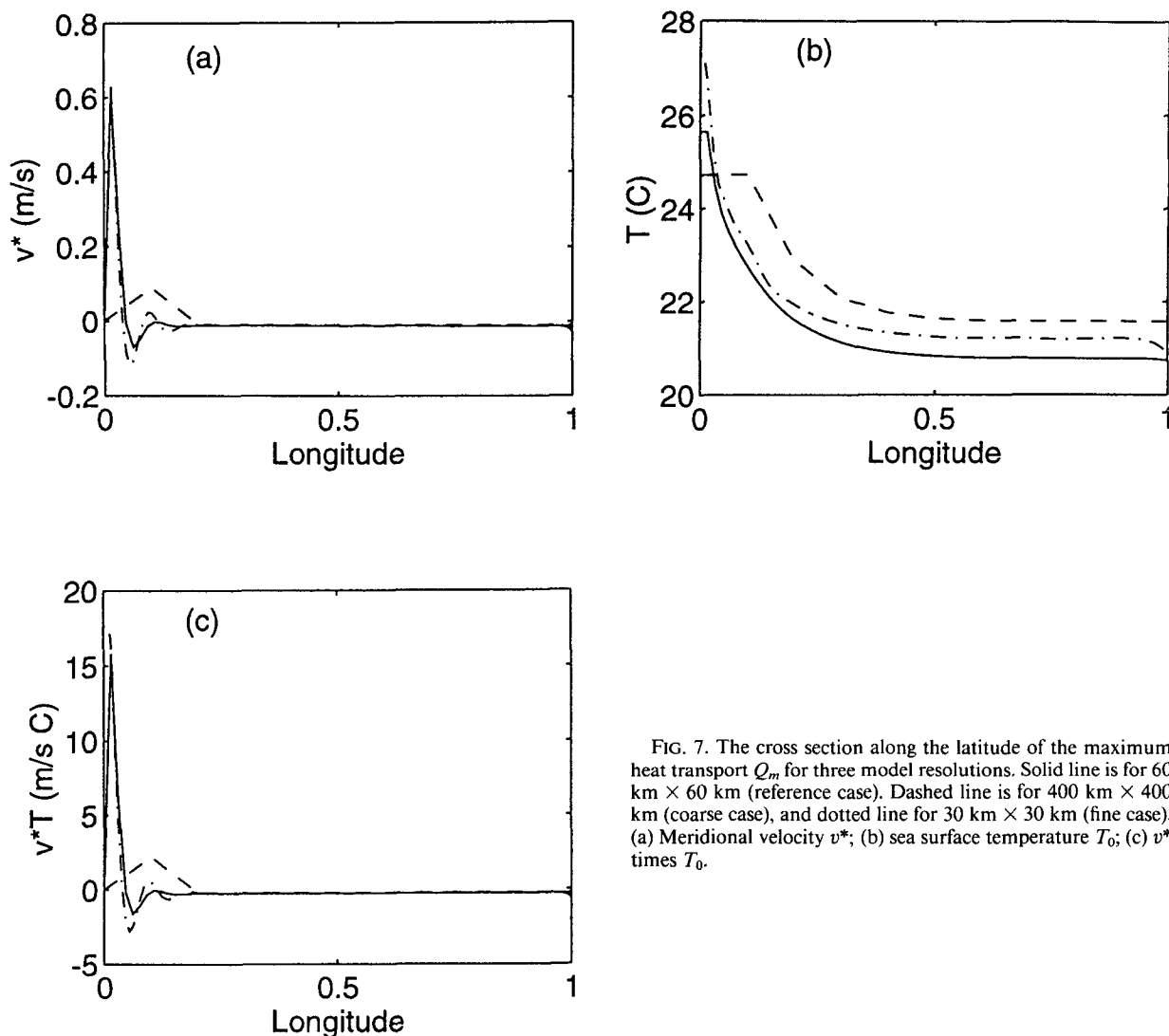


FIG. 7. The cross section along the latitude of the maximum heat transport Q_m for three model resolutions. Solid line is for 60 km × 60 km (reference case). Dashed line is for 400 km × 400 km (coarse case), and dotted line for 30 km × 30 km (fine case). (a) Meridional velocity v^* ; (b) sea surface temperature T_0 ; (c) v^*T .

that the heat transports increase very little when the resolution is greater than 60 km × 60 km. Therefore, we used the resolution of 60 km × 60 km for most of our sensitivity experiments.

d. Sensitivity to the basin width and other parameters

The scaling law showed that the heat transport is sensitive to the basin width, which may be important because the width of the Pacific at 24°N is nearly twice as large as that of the Atlantic, whereas observations show that the wind stress curl magnitudes in the two basins are almost the same (Trenberth et al. 1989). Thus, we designed an idealized Pacific-size model by doubling the reference basin width in the east–west direction, while keeping all other parameters (including the north–south extent of the basin and the 60-km grid

resolution) unchanged. The asymptotic steady equilibrium streamfunction of this experiment shows that the mass transport of the subtropical gyre is roughly doubled (Fig. 8). The variations of the maximum heat transport with the restoring timescale τ_d are shown in Fig. 9 for both the reference model and the double-width model. The maximum heat transport in the Pacific-size model reaches 0.73 PW, 228% of that in the reference model. This is consistent with the scaling results, which indicate that the heat transport would increase two to four times when the basin width is doubled. The restoring timescale corresponding to the maximum Q_m is about 2–3 months.

The scaling analysis showed that the sensitivity of the heat transport to the magnitude of the wind stress curl varies with λ , from a second power dependence for $\lambda \rightarrow \infty$, to independence for $\lambda \rightarrow 0$. The magnitude of the wind stress curl was halved and doubled, re-

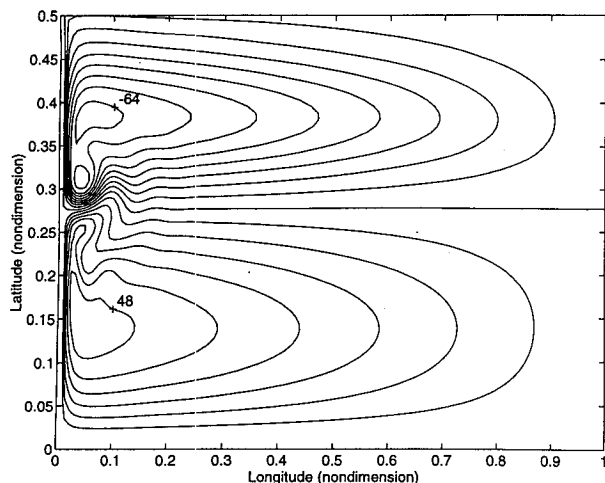


FIG. 8. The asymptotic steady streamfunction for the idealized Pacific-size model; Cl : 8 Sv.

spectively, with λ set to the standard value of 20 (see experiments 1, 5, and 6 in Table 1). Modeled heat transport is roughly proportional to the magnitude of the wind stress curl, consistent with the regime being intermediate to those of the two scaling analysis.

Four experiments were carried out for various meridional and zonal gradients of T_A . In both regimes $\lambda \rightarrow \infty$ and $\lambda \rightarrow 0$, the scales of the heat transports are proportional to the meridional gradient of T_A . This linear relation is confirmed approximately by the numerical experiments, which change the meridional gradient of T_A by $\pm 20\%$, respectively (see experiments 1, 7, and 8 in Table 1). Two experiments (experiments 9 and 10 in Table 1) were carried out to investigate the effect of zonal variations in T_A . A linear function of longitude is added to T_A , with an east-west temperature difference of $\pm 2^\circ$, respectively. If T_A on the western boundary is colder than that on the eastern boundary (experiment 9), the heat transport is reduced by 0.04 PW, while if it is warmer (experiment 10), it is increased by 0.06 PW. This indicates that the zonal variations in the atmospheric forcing affect the oceanic heat transport insignificantly, compared to the total oceanic transport found by Bryden et al. (1991), that is, 2 PW.

5. Summary and discussion

We have used a barotropic wind-driven oceanic circulation model coupled to a mixed-layer thermodynamic model to study the potential contribution of the wind-driven circulation to the poleward oceanic heat transport. Scaling analyses of the equations show two different regimes for the heat transport, characterized by $\lambda \rightarrow 0$ and $\lambda \rightarrow \infty$, where λ is the ratio between the ocean advection timescale and the restoring timescale of Newtonian cooling. The heat transport is pro-

portional to λ for small λ , and proportional to $1/\lambda$ as $\lambda \rightarrow \infty$. Numerical experiments show that the heat transport reaches its maximum when λ is near 20, which corresponds to a Newtonian restoring timescale of about 5 months for a barotropic ocean 500-m deep.

For the regime $\lambda \rightarrow \infty$, the air-sea interaction process dominates the heat budget. Thus the oceanic temperature is very nearly equal to the apparent atmospheric temperature. In this limit, the heat transport depends on the second power of the basin width. An increase in the basin width causes an increase in the Sverdrup mass transport, hence an increase in the western boundary current velocity. This, in turn, results in an increase in the zonal gradient of the ocean temperature. On the other hand, in the regime $\lambda \rightarrow 0$, the oceanic advection process dominates the heat budget, and the air-sea interface heat flux is relatively weak. Thus the temperature tends to be homogenized. The heat transport, in this asymptotic limit, is a linear function of the basin width and of the meridional gradient of the apparent atmospheric temperature T_A . The magnitude of the wind stress curl does not influence the heat transport in this limit because an increase/decrease of the boundary velocity, resulting from varied wind stress curl, is always compensated by a decrease/increase in the zonal gradient of the ocean temperature, and the heat transport is unchanged.

The scaling results agree, qualitatively, with our numerical experiments. The sensitivity of the heat transport to the boundary current velocity implies that a high resolution in the western boundary layer is necessary to simulate the heat transport accurately. Our numerical experiments have demonstrated that models with low resolution underestimate the heat transport, due to the weakness of the temperature advection by the western boundary current. If the resolution is sim-

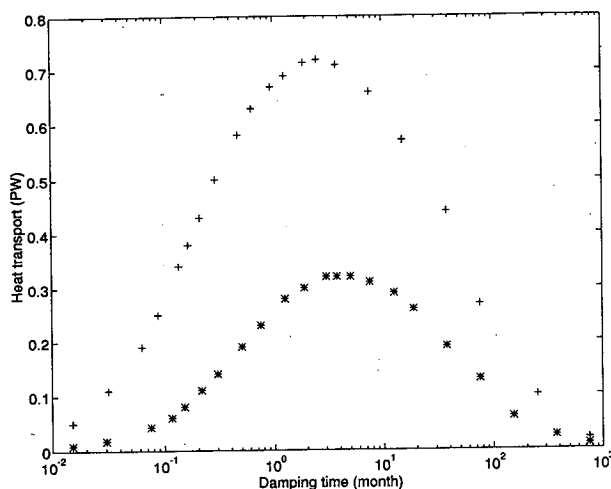


FIG. 9. Variation of the maximum heat transport Q_m with the Newtonian restoring time (in log coordinate). Cross dots are for Pacific-size run and star dots for the reference run (Atlantic size).

ilar to that used currently in global climate simulations, the heat transport is only about one-half of the high-resolution case. The numerical experiments have also shown that the zonal variations of the atmospheric forcing have little influence on the total oceanic poleward heat transport.

Our results allow some conclusions about the role of the wind-driven circulation in transporting heat poleward in the real oceans (assuming that diffusive heat transports are negligible). Using parameter values appropriate to the North Atlantic, our model can at most achieve only about 25% of the poleward heat transport observed in the North Atlantic at 24°N (1.2 PW, HB). This is consistent with the notion that the thermohaline circulation plays the dominant role in heat transport in the North Atlantic. On the other hand, with a doubled east–west extension of the model basin to resemble the North Pacific, our model yields a heat transport as large as 0.73 PW, which is close to the observed value at 24°N (Bryden et al. 1991). The good agreement is, however, fortuitous. First, if we used Haney's (1971) estimate of the Newtonian restoring time, the transport would be reduced to about 0.5 PW (see Fig. 9). Second, our model neglects the heat transport associated with the Ekman drift, which accounts for about half the Pacific heat transport at 24°N (Bryden et al. 1991). The omission of this transport is in part compensated by our model's overestimate of the mass transport below the Ekman layer at 24°N. Nevertheless, our results, along with the lack of deep water formation in the North Pacific (Warren 1983), confirm that the wind-driven circulation is probably the main agent that transports heat poleward in the North Pacific.

Acknowledgments. Eighty percent (\$40,000) of this research was funded by the U.S. Department of Energy's (DOE) National Institute for Global Environmental Change (NIGEC) through the NIGEC Northeast Regional Center at Harvard University (DOE Cooperative Agreement No. DE-FC03-90ER61010). The remainder was supported by the National Science Foundation. Financial support does not constitute an endorsement by DOE or NSF of the views expressed in this article. We thank John Marshall for suggesting an efficient Poisson solver.

REFERENCE

- Anderson, D., K. Bryan, A. Gill, and R. Pacanowski, 1979: The transient response of the North Atlantic: Some model studies. *J. Geophys. Res.*, **84**, 4795–4815.
- Blandford, R. R., 1971: Boundary conditions in homogeneous ocean models. *Deep-Sea Res.*, **18**, 739–751.
- Bryan, F., and W. R. Holland, 1989: A high resolution simulation of the wind- and thermohaline-driven circulation in the north Atlantic Ocean. *Parameterization of Small Scale Process*, P. Muller, Ed., Hawaii Institute of Geophysics, 99–115.
- Bryan, K., 1963: A numerical investigation of a nonlinear model of a wind-driven ocean. *J. Atmos. Sci.*, **20**, 594–606.
- , and M. Cox, 1968: A nonlinear model of an ocean driven by wind and differential heating: Part I. Description of the three-dimensional velocity and density fields. *J. Atmos. Sci.*, **25**, 945–967.
- , and L. J. Lewis, 1979: A water mass model of the World Ocean. *J. Geophys. Res.*, **84**, 2503–2517.
- Bryden, H., D. H. Roemmich, and J. A. Church, 1991: Ocean heat transport across 24°N in the Pacific. *Deep-Sea Res.*, **38**, 297–324.
- Bye, J., and G. Veronis, 1980: Poleward heat flux by an ocean gyre. *Dyn. Atmos. Oceans*, **4**, 101–114.
- England, M. H., 1993: Representing the global-scale water masses in ocean general circulation models. *J. Phys. Oceanogr.*, **23**, 1523–1552.
- Hall, M. M., and H. Bryden, 1982: Direct estimates and mechanisms of ocean heat transport. *Deep-Sea Res.*, **29**, 339–359.
- Haney, R. L., 1971: Surface thermal boundary condition for ocean circulation models. *J. Phys. Oceanogr.*, **1**, 241–248.
- Huynh, Q., and G. Veronis, 1981: The effect of temperature-dependent exchange coefficients on poleward heat flux by oceanic gyres. *Dyn. Atmos. Oceans*, **6**, 49–66.
- Manabe, S., and R. Stouffer, 1988: Two stable equilibria of a coupled ocean–atmosphere model. *J. Climate*, **1**, 841–866.
- Marotzke, J., 1994: Ocean models in climate problems. *Ocean Processes in Climate Dynamics: Global and Mediterranean Examples*, P. Malanotte-Rizzoli and A. R. Robinson, Eds., Kluwer Academic, 79–109.
- Marshall, J., 1984: Eddy-mean-flow interaction in a barotropic ocean model. *Quart. J. Roy. Meteor. Soc.*, **110**, 573–590.
- Moro, B., 1988: On the nonlinear Munk model. Part I. Steady flows. *Dyn. Atmos. Oceans*, **12**, 259–287.
- Rintoul, S. R., and C. Wunsch, 1991: Mass, heat, oxygen and nutrient fluxes and budgets in the North Atlantic Ocean. *Deep-Sea Res.*, **38**, S355–S377.
- Roemmich, D., and C. Wunsch, 1985: Two transatlantic sections: Meridional circulation and heat flux in the subtropical North Atlantic Ocean. *Deep-Sea Res.*, **32**, 619–664.
- Trenberth, K. E., J. G. Olson, and W. G. Large, 1989: A global ocean wind stress climatology based on ECMWF analyses. NCAR Tech. Note NCAR/TN-338+STR, 23–28.
- Veronis, G., 1966: Wind-driven circulation. Part II: Numerical solutions of the non-linear problem. *Deep-Sea Res.*, **13**, 31–55.
- Warren, B., 1983: Why is no deep water formed in the North Pacific? *J. Mar. Res.*, **41**, 327–347.